ACS Photonics

pubs.acs.org/journal/apchd5

Article

Micromirror Total Internal Reflection Microscopy for High-Performance Single Particle Tracking at Interfaces

Xuanhui Meng,[§] Adar Sonn-Segev,[§] Anne Schumacher, Daniel Cole, Gavin Young, Stephen Thorpe, Robert W. Style, Eric R. Dufresne, and Philipp Kukura*

Cite This: *ACS Photonics* 2021, 8, 3111−3118

Read Online

ACCESS | Metrics & More | Article Recommendations | Supporting Information

ABSTRACT: Single particle tracking has found broad applications in the life and physical sciences, enabling the observation and characterization of nano- and microscopic motion. Fluorescence-based approaches are ideally suited for high-background environments, such as tracking lipids or proteins in or on cells, due to superior background rejection. Scattering-based detection is preferable when localization precision and imaging speed are paramount due to the in principle infinite photon budget. Here, we show that micromirror-based total internal reflection dark field microscopy enables background suppression previously only reported for interferometric scattering microscopy, resulting in nanometer localization precision at 6 μs exposure time for 20 nm gold nanoparticles with a 25 × 25 μm^2 field of view. We demonstrate the capabilities of our implementation by characterizing sub-nanometer deterministic flows of 20 nm gold nanoparticles at liquid−liquid interfaces. Our results approach the optimal combination of background suppression, localization precision, and temporal resolution achievable with pure scattering-based imaging and tracking of nanoparticles at interfaces.

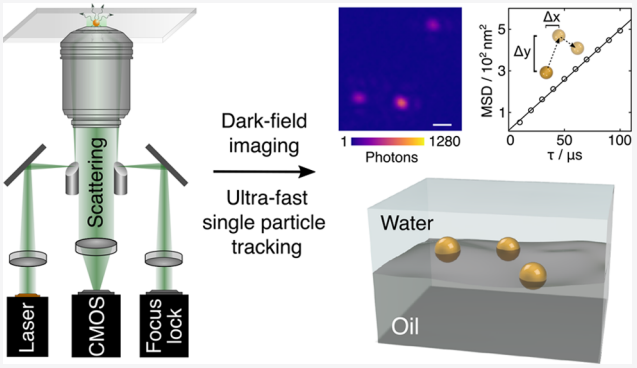

KEYWORDS: *total internal reflection, dark field microscopy, single particle tracking, light scattering, nanoparticles at fluid interfaces, colloidal flow at fluid interfaces*

INTRODUCTION

The ability to follow the motion of nanoscopic objects fundamentally relies on their detection and the precision with which we can determine the position of the object of interest for a given integration time.[1] This localization precision is important for defining the smallest measurable real motion, as opposed to positional fluctuations arising from fitting a signal with finite noise,[2] while the integration time determines the type of motion that can be observed, in an extreme reaching the ballistic limit.[3,4] While fluorescence-based approaches have many advantages in the context of specificity and background suppression, they face limitations at the extremes of localization precision and temporal resolution when using small labels. For single emitters, the fundamental photophysics limits photon emission rates to about 1 MHz if trajectories of appreciable length are to be recorded (≫ms). Coupled with limited detection efficiencies of even the best microscopes, detecting even 1 photon/μs is therefore a formidable task, although these limitations have been recently mitigated by the introduction of MINFLUX.[5] Larger objects or multiemitter systems can be used,[6] although for labels on the order of 40 nm or more one begins to resolve label motion in addition to the motion of the labeled object, thus requiring temporal averaging back to the ms regime in order to maintain the desired localization precision.[7] An additional limitation for fluorescence imaging arises from photobleaching, which limits the observation time. Photostability decreases with increasing illumination power, making trajectories shorter the faster and more precise the measurement that is required.

One solution to these limitations involves the use of nanoscopic scatterers, which possess greater photostability compared to fluorescent labels. Metallic nanoparticles are ideally suited as scattering labels in the visible regime because they exhibit a plasmon resonance, where their polarizability and thus scattering cross sections are significantly enhanced.[8] With such labels and improvements to microscope design, nanometer-precise tracking on the microsecond time scale has become routine, reaching 1.3 nm localization precision at 55 μs temporal resolution with 40 nm gold nanoparticles

Received: August 20, 2021
Published: October 8, 2021

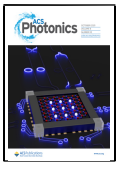

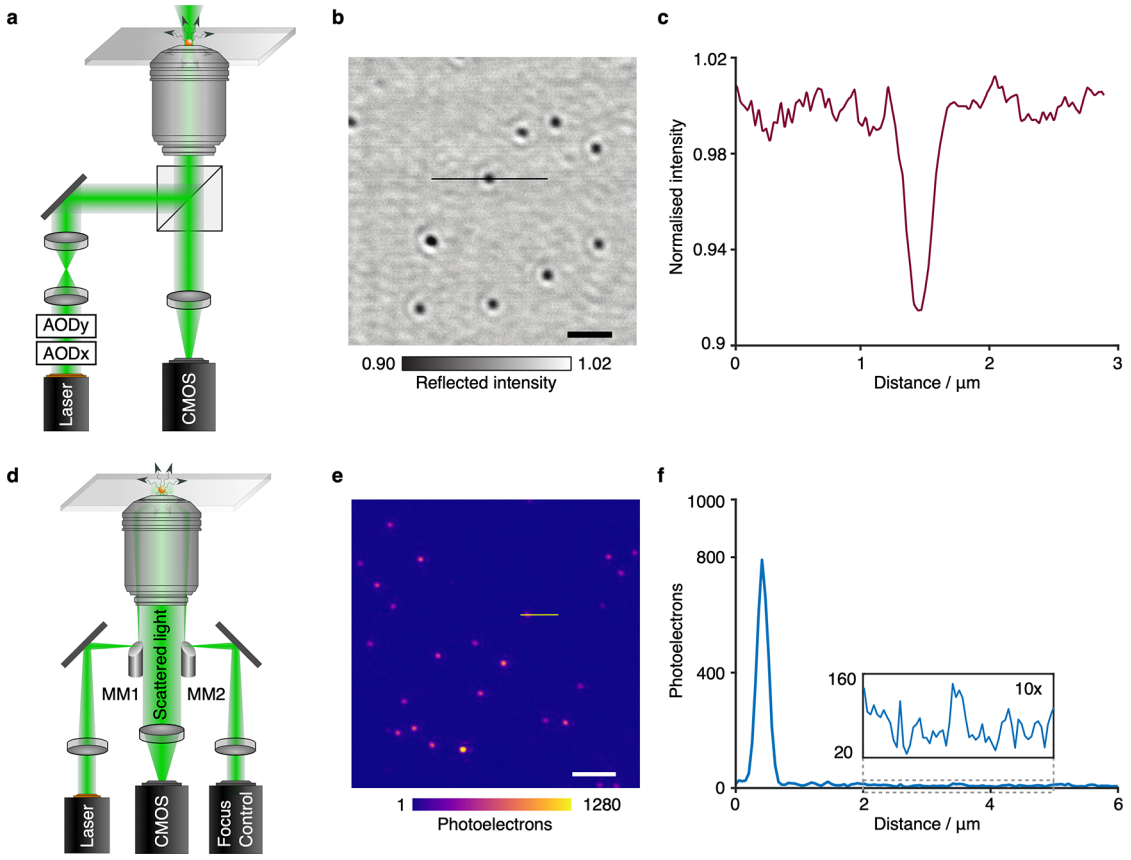

Figure 1. Comparison of interferometric scattering (iSCAT) and micromirror based total internal reflection scattering microscopy. (a) Schematic illustration of an AOD-based iSCAT microscope. (b) Typical iSCAT image of 20 nm AuNPs immobilized on a cover glass surface immersed in water. Scale bar: 1 μm. (c) Linecut across the particle in (b). (d) Objective-type TIR using two micromirrors. (e) Respective image of 20 nm AuNPs immobilized on cover glass. Scale bar: 2 μm. (f) Linecut of a single particle in (e), including a zoom of the imaging background. AOD: Acousto-optic deflectors. MM: Micromirror.

(AuNPs).[7,9] Background suppression using dark-field imaging can in principle be improved to detect even single molecule fluorescence,[10] although the more traditional objective-type approaches have struggled with sufficient background suppression to enable high localization precision with 20 nm labels.[11] Interferometric scattering microscopy (iSCAT) enables observation of even smaller labels, for example reaching 2 nm localization precision with 2 μs temporal resolution with 20 nm diameter AuNPs.[12]

Despite the unique capabilities of iSCAT,[13,14] objective-type dark-field imaging has some potential advantages in the context of single particle tracking: 1. Sample illumination is limited to the first few hundred nanometers near the glass−water interface, reducing both the power load on the bulk sample and background features from scatterers above the interface. 2. High-speed tracking (<ms) with iSCAT requires a stationary illumination beam, which usually limits the field of view to about a < 10 μm fwhm if interference fringes caused by focusing the illumination beam into the objective are to be avoided.[15] 3. Objective-type total internal reflection illumination enables trivial combination with total internal reflection fluorescence imaging as the illumination beam is already provided. 4. The linear scaling of the detected signal for iSCAT with the volume of the scatterer compared to a squared dependence for dark-field detection also implies that a sample-specific background that is smaller than the signal of interest plays a more significant role in iSCAT than in dark-field imaging.[16] Conversely, iSCAT is intrinsically more suited to simultaneously imaging a larger range of particle sizes for a given dynamic range in detection.

The last point is illustrated by considering an iSCAT (Figure 1a) image of 20 nm AuNPs on microscope cover glass immersed in water (Figure 1b). Individual AuNPs appear as dark spots on top of a speckle-like background, with a signal-to-background ratio of ∼10 (Figure 1c), irrespective of the experimental implementation.[12,17,18] The speckle-like background likely stems from surface imperfections of microscope cover glass, as illustrated when using atomically flat mica surfaces[19] or refractive index matching.[20] While this background can be subtracted computationally,[21] it limits the visibility of small particles and can cause artifacts in localization. A dark-field image of the same sample could thus, at least in principle, exhibit a 100:1 signal-to-background ratio because of the difference in signal scaling, assuming that the spurious background from the illumination can be suppressed to the level of the coverglass-induced scattering.

RESULTS

Background light in dark-field microscopy can be generally attributed to two sources: spurious reflections from optics and scattering from or near the illuminated surface itself (Figure S1b). The achievable signal-to-background ratio in iSCAT (Figure 1b) indicates that the latter can be suppressed significantly below the signal that can be obtained from a 20

https://doi.org/10.1021/acsphotonics.1c01268
ACS Photonics 2021, 8, 3111−3118

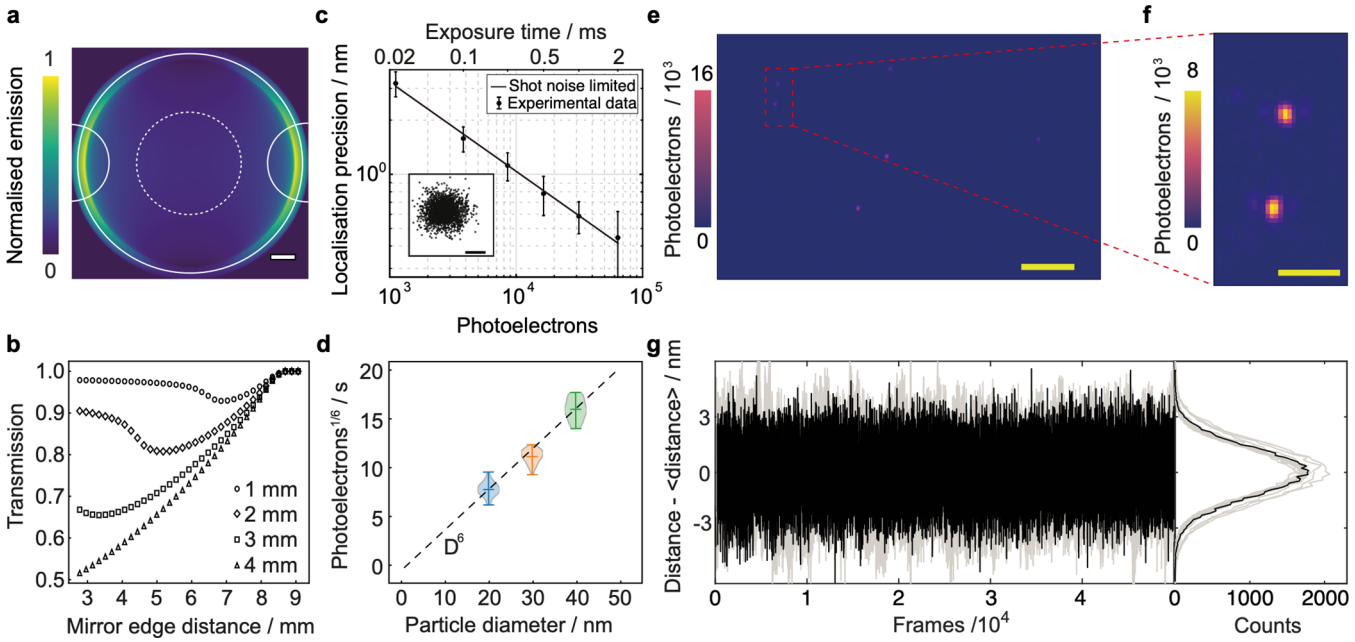

Figure 2. Performance of the micromirror microscope. (a) Simulated back focal plane emission pattern of a single emitter at a glass (n = 1.52) − water (n = 1.33) interface. The objective pupil (NA = 1.42, Back aperture = 8.52 mm) and micromirrors are indicated by white solid lines. The aperture of a 4 mm diameter perforated mirror is shown by white dashed lines. (b) Transmission as a function of mirror size and separation for the objective and mirrors shown in (a). (c) Theoretical shot-noise limited behavior (line) and experimental localization precision measured by varying the camera exposure time at 2.7 kW/cm^2 illumination intensity. Inset: Scatter plots of a 20 nm AuNP immobilized directly on microscope cover glass imaged at 6 μs exposure time. Scale bar: 1.5 nm. (d) Measured photoelectron flux per second vs particle size, and comparison to the expected D^6 scaling. Data were acquired starting with 40 nm particles, increasing exposure time by a factor of 5.6 and 64 for 30 and 20 nm particles, respectively, and then calculating the total number of detected photoelectrons/s. (e) A representative image of immobilized 20 nm AgNPs used for calculating the localization precision. Image acquired at 100 kHz with 8 μs exposure time. The distance of each particle pair is measured for each image in the movie, and the localization precision is calculated from the distance fluctuations. Scale bar: 4 μm. (f) Zoom on one particle pair from (e). Scale bar: 1 μm. (g), Fluctuations of the distance between particle pairs, shifted by each pair mean distance to overlay all pairs. Traces of all frames of the movie (left) and their corresponding histogram (right). These traces and histograms refer to the analysis of the image and movie presented in (e) and (f). Dark lines correspond to the particle pair shown in (f). Light lines correspond to the other pairs in the image in (e).

nm AuNP. Given the extreme levels of background rejection achieved previously by a beam stop placed closely to the entrance pupil,[10] we reasoned that using two small mirrors to couple illumination light in and out of the objective in an objective-type TIR arrangement (Figure 1d and Figure S1a) should be able to achieve similar levels of background suppression upon optimization of the mirror sizes and position, even though recent implementations were limited to observation of 40 nm diameter AuNP, as standard for darkfield microscopy.[22,23] In this experimental arrangement, the main source of background light must thus originate from reflections caused by the lenses contained within the high numerical aperture objective, which could be captured efficiently by mirrors placed near the entrance pupil for both the incident and reflected beam.

A dark-field image of 20 nm diameter AuNPs on a standard glass coverslip immersed in water acquired with a setup using a 3 mm diameter mirrors setup exhibited much lower background compared to the nanoparticle signal (Figure 1e) than in the corresponding iSCAT image (Figure 1b). The signal to background ratio now approaches 100:1 as expected when viewed both for individual particles (Figure 1f) and across the field of view (Figure 1f inset). The limiting background is likely caused by coverslip surface roughness as for iSCAT, since it translates when the sample is translated laterally. The key trade-off is between mirror size and position to reduce stray light while minimizing loss of scattered light caused by partial blockage of the objective back aperture. To quantify this relationship, we calculated the scattering pattern of a nanoparticle at the glass/water interface at the exit pupil of the objective for s-polarized illumination (Figure 2a).[24−26] The high emission density at high numerical apertures can be attributed to the refractive index mismatch between glass and water, and illustrates the advantage of using two small mirrors for coupling illumination light compared to a perforated mirror as described previously[11] in terms of collection efficiency. For instance, a mirror with a central aperture of 4 mm diameter combined with an objective with an 8.5 mm diameter entrance pupil would transmit only 15% of collected light.

We then investigated the transmission of a dual mirror approach as a function of both mirror size and position. For the 60× oil immersion objective we use here, a 3 mm diameter mirror enables >65% transmission of scattered light irrespective of the mirror position (Figure 2b). We placed our micromirrors within 5 mm of the entrance pupil along the optical axis, which was the closest practical distance achievable, and at a center-to-center separation of 8.3 mm centered on the entrance pupil. For this arrangement, we expect 94% of scattered light collected by the objective to reach the tube lens and ultimately the camera, enabling highly efficient collection. We found excellent agreement between shot noise limited and experimentally determined performance (Figure 2c), evaluated by quantifying interparticle distances (Figure 2e−g). Detecting ∼900 photons at 250 μs exposure time agrees well with the estimated detection efficiency of our setup (40%), the incident power density, and the scattering cross section of 20 nm

https://doi.org/10.1021/acsphotonics.1c01268
ACS Photonics 2021, 8, 3111−3118

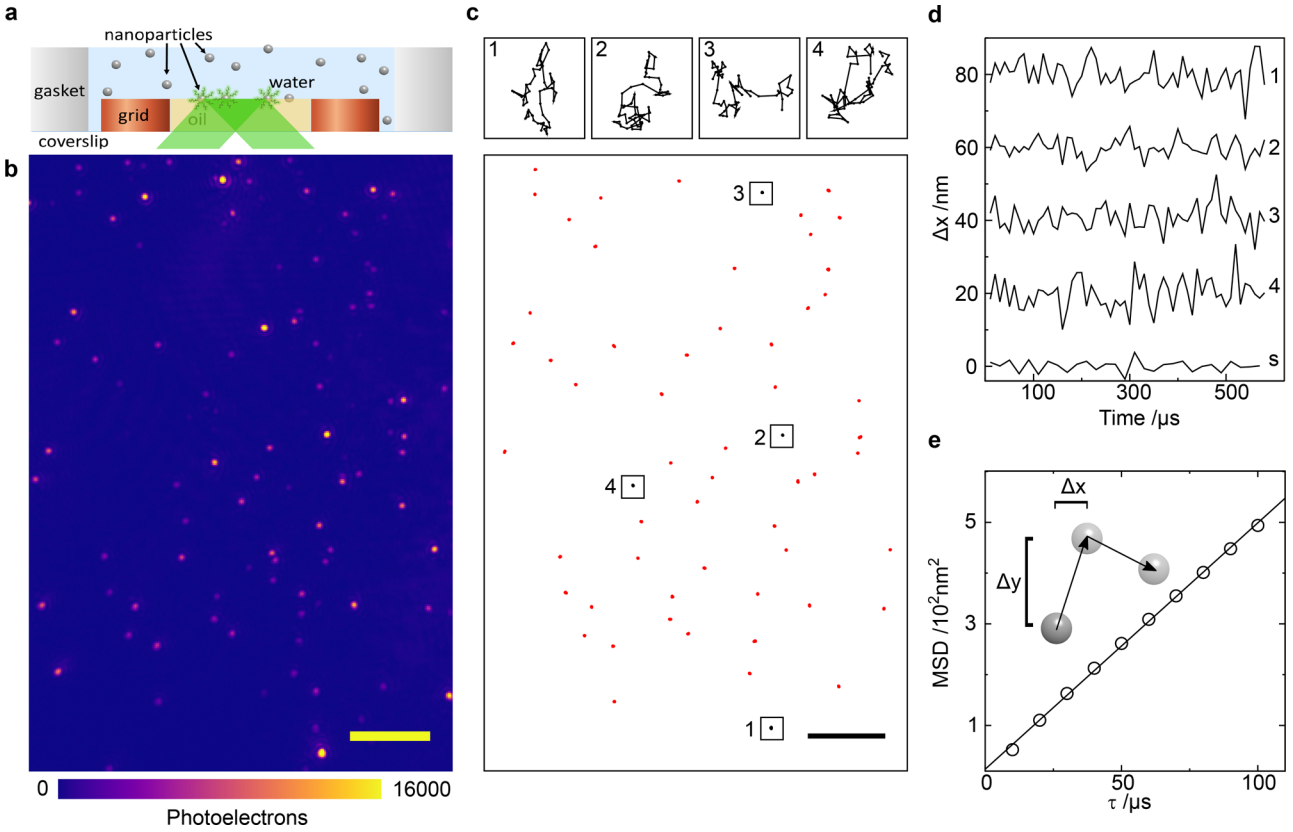

Figure 3. High speed diffusion of metallic nanoparticles at oil−water interfaces. (a) Schematic illustration of the experimental system: nanoparticles (NPs) are dispersed at an oil−water interface. (b) Representative image of 20 nm AgNPs diffusing at the interface. Scale bar: 4 μm. (c) Trajectories of 20 nm AgNPs acquired at 100 kHz during the illumination period (in total 60 frames), and zoom of 4 trajectories. Scale bar: 4 μm. (d) Step-sizes along the x-axis, Δx for the 4 zoomed trajectories in (c). The Δx traces are shifted vertically for clarity. The bottom trace corresponds to an immobilized particle on glass (s). (e) Ensemble and time-averaged mean square displacement (MSD) of 20 nm AgNPs at an oil−water interface vs lag-time τ (data taken at 100 kHz). The black line represents a linear fit, MSD = $4D_s\tau$, to the data. Inset: Illustration of particle diffusion.

diameter AuNPs in water (~3 nm^2).[27] The fitted distribution of center of mass (Figure 2c) of an immobilized 20 nm AuNP on a microscope cover glass acquired with a 6 μs exposure time falls approximately within a 4 nm circle in diameter, which demonstrates a low level of localization error. We further verified the single particle nature of our data by confirming the D^6 scaling of the scattering intensity for nominally 20, 30, and 40 nm diameter AuNPs (Figure 2d). To quantify the maximum achievable combination of localization precision and temporal resolution with our setup, we acquired a series of images of 20 nm silver nanoparticles (AgNPs) immobilized on glass with 8 μs exposure time (Figure 2e,f) at a 100 kHz frame rate, and evaluated the interparticle distance for an incident power density of 30 kW/cm^2. We chose the interparticle distance as a reliable measure of localization precision to avoid mistaking sample vibrations for localization error. The interparticle distance fluctuations resulted in a Gaussian distribution with a fwhm of 2.9 nm (SD 1.23 nm) (Figure 2g), yielding a single particle localization precision of 0.9 nm under these imaging conditions.

To evaluate the performance of our microscope in a challenging single-particle tracking context, we chose nanoparticles at fluid interfaces, which are an attractive experimental system for studying fundamental questions in condensed matter physics such as the structure and dynamics of confined fluids and phase behavior of 2D systems. In addition, nanoparticles at interfaces have various technological applications including emulsification, assembly of nanocomposites with tunable properties and construction of nanostructured membranes for filtration.[28−31] The phenomenon of solid particles adsorbing to soft deformable interfaces, thereby providing them with resistance against coalescence, is well-known,[32,33] and occurs as a result of the reduction in free energy with respect to the bare interface, as in the case of molecular surfactants. The gain in free energy scales with particle size,[34] and thus the stability of nano- and microsized particles at the interface increases compared to molecular surfactants. Microparticles are adsorbed irreversibly to interfaces with desorption energies of ~$10^8 k_BT$ (the thermal energy). Nanoparticles experience much lower desorption energies of 5−100 k_BT depending on the size and surface chemistry of the particles.[34,35] The weaker stability of nanoparticles at the interfaces results in a much richer observable energy surface,[36] with short-lived metastable states. Imaging at low frame rates of 50 Hz, with exposure times on the millisecond time scale, enables the observation of time-averaged behavior. Imaging at much faster frame rates (10−100 kHz) without compromising the precision opens the possibility to resolve and quantify the more complex potential energy landscapes of these systems.

We thus dispersed AuNPs and AgNPs at the interface between water and a high refractive index (n = 1.523) oil (Figure 3a). The high density and refractive index of the oil compared with the microscope cover glass allowed for total

https://doi.org/10.1021/acsphotonics.1c01268
ACS Photonics 2021, 8, 3111−3118

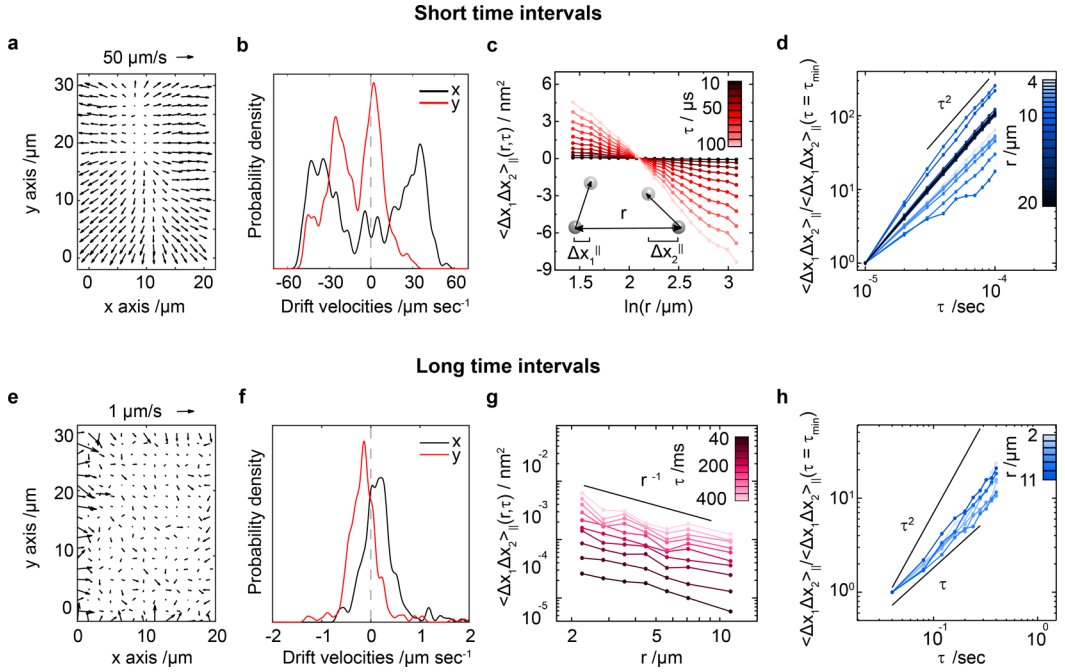

Figure 4. Small-scale effects of nanoparticle diffusion at the oil−water interface. (a−d) Short time intervals: (a) Displacement field of 20 nm AgNPs at 100 kHz. Scale bar 50 μm/s. (b) Probability density of the average velocities from (a) along x (black) and y (red). (c and d) Two-point displacement correlation at oil−water interfaces for 20 nm AgNPs, imaged at 100 kHz. (c) Longitudinal displacement correlation as a function of the logarithm particle separation, ln(r), for 10 different lag times, τ = 10−100 μs. (d) Replotting the displacement correlation for each r as a function of τ. Plots are normalized to the first data point (i.e., value at the minimum lag time, τ_{min}) for clarity. (e−h) Long-time intervals: (e) Displacement field of 20 nm AgNPs at 50 Hz. Scale bar 1 μm/s. (f) Probability density of the average velocities from (e) along x (black) and y (red). (g) Longitudinal displacement correlation as a function of r, for different lag times between τ = 0.04−0.4 s. (h) Replotting the displacement correlation for each r as a function of τ. Plots are normalized as for (d).

internal reflection to occur at the liquid−liquid interface. To enable imaging at high frame rates with nanometer precision while ensuring minimal sample heating, we illuminated in a stroboscopic fashion with a 3.5−5% duty ratio. Each cycle included a dark period of several milliseconds, and an illuminated period of approximately 1 ms, during which one movie of nanoparticle dynamics at the interface was recorded. Each movie included 10−60 frames, and ∼4000 consecutive short movies were recorded and saved in one file. In this way, we could generate high contrast dark field images even at very short exposure times (Figure 3b), enabling single particle tracking of tens of particles with simultaneous ∼1 nm spatial precision and 10 μs temporal resolution. The particles exhibited differences in their detected intensities (Figure 3b and Figure S3) due to size variations and the D^6 dependence of the scattering intensity. Individual trajectories of 20 nm diameter AgNPs showed diffusive motion, in contrast to immobilized AgNPs (Figure 3c, d), where we can eliminate any influence from vibrations (Figure S4). The nanoparticle motion appeared diffusive, evidenced by the linear increase of the mean-squared displacement (MSD) with the lag time, τ, as expected for conventional single particle diffusion (Figure 3e). In addition, we found no signatures of structuring of the particles at the oil−water interface, evident from the pair correlation function (Figure S5).

To further characterize the nature of the nanoparticle motion at the interface with short lag times, we quantified the spatial dependence of single particle displacements (Figure 4a). Although the particle trajectories and MSD appear diffusive, the vector field at short lag times (τ = 10 μs) revealed an outward flow pattern with drift displacements smaller than 0.5 nm, corresponding to a drift velocity of 50 μm/s (Figure 4b). While conventional Brownian motion would result in Gaussian distributions centered on zero, these velocity distributions show two well-resolved peaks at nonzero speeds. Interestingly, this behavior persists for different particle concentrations, with faster speeds at higher particle concentrations (Figure S6).

Deterministic flows at fluid−fluid interfaces[37] can be driven by nonuniform surface tensions. This effect is termed Marangoni flow and typically arises from temperature or surfactant concentration gradients. Here, the absorption of the laser illumination by AgNPs drives local heating. In the Supporting Information, we show that a temperature difference as small as 1 mK degrees over the 10 μm field-of-view is sufficient to drive the observed flow. This hypothesis is supported by the observation that the flow speed increases at higher particle concentrations (Figure S6).

To further demonstrate that this behavior is an interfacial effect rather than a bulk one, we analyzed the correlated motion of pairs of particles, which allows us to observe the fluid-mediated interactions between particles. For that purpose, we quantified the ensemble-averaged longitudinal (∥) displacement correlations of particle pairs as a function of interparticle distance r and lag time τ[38]

$$\langle \Delta x_1 \Delta x_2 \rangle_{\parallel} \equiv \langle \Delta x_i^{\parallel}(t, \tau) \Delta x_j^{\parallel}(t, \tau) \delta(r - R_{ij}(t)) \rangle$$

where $\Delta x_i^{\parallel}(t, \tau)$ is the displacement of particle i between time t and $t + \tau$, projected parallel to the line connecting the pair, and $R_{ij}(t)$ is the pair separation at time t (see also inset of Figure 4c). The angular brackets represent averages over all times t and particle pairs $i \neq j$. In systems where the momentum can

https://doi.org/10.1021/acsphotonics.1c01268
ACS Photonics 2021, 8, 3111−3118

travel in three dimensions, these correlations should decay as $\sim 1/r$. For diffusive motion these correlations are expected to increase linearly with τ, similar to the MSD. Intriguingly, at short time intervals, the longitudinal displacement correlations scale as $\sim \ln(1/r)$, characteristic of interface-dominated behavior[39−41] (Figure 4c), where momentum travels only in two dimensions. Replotting the displacement correlation for each r as a function of τ shows superdiffusive scaling, in the vicinity of the ballistic limit, which scales with $\sim \tau^2$ (Figure 4d). This reflects the dominance of deterministic outward motion (Figure 4a). The plots in Figure 4d are normalized by their initial value (i.e., value at the minimum lag time, τ_{min}) to simplify presentation. Similar behavior was observed for 20 and 30 nm AuNPs (Figure S7).

Operating with stroboscopic illumination allowed us to study the particle motion at both short (10−100 μs) and long (40−400 ms) lag times, simultaneously. In the long lag-time movies, the laser illuminated the sample for less than 5% of the total lag time, allowing the system to equilibrate and any local heating to dissipate to the bulk. Therefore, at long lag times we observed no apparent flows (Figure 4e), with drift velocities less than 1 μm/s, distributed around zero (Figure 4f). This indicates that the system had sufficient time to equilibrate during the dark period. In accordance, the displacement correlation curves exhibit normal diffusive behavior with an r^{-1} decay (Figure 4g) and linear time dependence (Figure 4h). These results indicate that the viscous response at the interface is mediated by the two bulk fluids (oil and water) rather than the interface, as anticipated (see Supporting Information for a full derivation of the expected viscous response).

We further analyzed the displacement correlations at short lag times (Figure 4c) to separate the deterministic behavior, which scales as $\sim \tau^2$, from the diffusive (viscous) behavior, which scales as $\sim \tau$ (Figure S8, Supporting Information for analysis details). Extraction of the correlated diffusive coefficients provides a means to estimate the effective viscosity at the interface, related to the flows at and close to the interface. For large nanoparticle separations, the leading term of this effective viscosity should be only influenced by the properties of the two bulk fluids (and not the interface), with each fluid contributing equally, i.e., insensitive to the exact lateral position of the particle within the interface. Therefore, the effective viscosity is expected to be the average viscosities of the two bulk fluids (see Supporting Information for the full derivation). This viscosity is different from the local viscosity extracted from self-diffusion of particles, which is sensitive to the exact position of the particles at the interface (i.e., their immersion depth or three-phase contract angle). The effective viscosity values were approximately the average between the oil and water viscosities (0.044 and 0.00095 Pa·s, respectively), corresponding to 0.0241 ± 0.003 (20 nm AgNPs), 0.0227 ± 0.0034 (20 nm AuNPs), and 0.0244 ± 0.004 (30 nm AuNPs) Pa·s. These values agree with the theoretical prediction based on Green's functions at fluid−fluid interfaces (see Supporting Information and Figure S9).

DISCUSSION

Our results demonstrate that micromirror-based TIR microscopy, when optimized in terms of mirror size and position, can suppress background light toward the minimum set by the sample interface while maintaining very high light collection efficiency. In the context of using light scattering for single particle tracking applications at interfaces in the absence of significant additional scattering, such as provided by cells for example, our approach yields a number of key advantages over the state-of-the art. In comparison to reported implementations of TIR scattering microscopy,[9,11] we demonstrate high SNR detection of 20 nm AuNPs only limited by the scattering background cause by surface roughness, enabling SNRs on the order of 50 (Figure 1f). The ability to perform such high background suppression is important, because large particles can induce localization noise as they move about their molecular linker, which ultimately leads to lower temporal resolution.[7] Background suppression toward the minimum set by the sample at least in principle allows extreme detection sensitivity, as demonstrated in mass photometry for example.[42] In comparison to interferometric methods, such as iSCAT, our approach similarly provides distinct advantages. Owing to TIR, the incident power does not pass through the sample, which reduces both out of focus scattering and overall sample heating. Finally, the D^6 scaling of signal intensity results in a larger SNR for small scattering labels over the background enabling higher localization precision and smaller localization error induced by the underlying roughness.[43] Taken together, these capabilities allow for some of the highest combination of localization precision, temporal resolution, and incident power density for nanoscopic scattering imaging.

To demonstrate the capabilities of our microscope, we selected a system of nanoparticles at an oil−water interface. We were able to record the motion of AuNPs and AgNPs on the 10−100 μs time scale (high frame rates of 10−100 kHz), and a large field of view of tens of μm^2, thus capturing the trajectories of tens of nanoparticles simultaneously. Moreover, our stroboscopic illumination approach allowed us to also simultaneously record particle motion at longer time intervals of tens of ms. At short time intervals the averaged MSD suggests particles exhibit diffusive behavior. However, further analysis of the particles' motion revealed spatial correlations and a deterministic motion which emerged on top of the diffusive one. We linked the latter behavior to thermal Marangoni flows, which decay within a few milliseconds once the illumination is turned off and therefore are not present at long time intervals. In addition, we could separate the diffusive and deterministic contributions of the displacement correlation behavior. The diffusive contribution to the correlations at large particle separations is in excellent agreement with theoretical predictions, described in the Supporting Information. According to these calculations, the effective viscosity of this mode should be equal to the average viscosity of the two phases. The effective viscosity of this mode was found to be 0.0237 ± 0.0035 Pa·s, while the average viscosity of the two phases is 0.0225 Pa·s.

Taken together, these results demonstrate that micromirror darkfield microscopy can achieve background suppression toward the limits previously reported with iSCAT and can be used for ultrahigh performance particle imaging and tracking. For low background tracking applications, such as those on microscope cover glass including supported lipid bilayers or molecular motors, where scattering labels producing signals comparable to 20 nm AuNPs can be used, our approach may prove to be the preferred choice due to its combination of detection efficiency, background suppression, field of view, and achievable imaging speed.

https://doi.org/10.1021/acsphotonics.1c01268
ACS Photonics 2021, 8, 3111−3118

■ ASSOCIATED CONTENT

Supporting Information

The Supporting Information is available free of charge at https://pubs.acs.org/doi/10.1021/acsphotonics.1c01268.

Materials, microscope alignment, focus control, calculation of scattered light transmission, localization precision (LP) calculation, data acquisition and setup adaptation, microscope coverslip cleaning procedure, preparation of oil−water interfaces, vibration analysis of the experimental setup, estimate of temperature gradient required to drive the observed flow, separation of deterministic and diffusive contributions to displacement correlation, pair correlation function g(r), derivation of viscous response at fluid interfaces for large particle separations, supplementary Figures S1−S9, references (PDF)

■ AUTHOR INFORMATION

Corresponding Author

Philipp Kukura − *Physical and Theoretical Chemistry Laboratory, Department of Chemistry, University of Oxford, Oxford OX1 3TA, U.K.;* orcid.org/0000-0003-0136-7704; Email: philipp.kukura@chem.ox.ac.uk

Authors

Xuanhui Meng − *Physical and Theoretical Chemistry Laboratory, Department of Chemistry, University of Oxford, Oxford OX1 3TA, U.K.*

Adar Sonn-Segev − *Physical and Theoretical Chemistry Laboratory, Department of Chemistry, University of Oxford, Oxford OX1 3TA, U.K.*

Anne Schumacher − *Physical and Theoretical Chemistry Laboratory, Department of Chemistry, University of Oxford, Oxford OX1 3TA, U.K.*

Daniel Cole − *Physical and Theoretical Chemistry Laboratory, Department of Chemistry, University of Oxford, Oxford OX1 3TA, U.K.;* Present Address: Refeyn Ltd., 1 Electric Avenue, Ferry Hinksey Road, Oxford OX2 0BY, U.K

Gavin Young − *Physical and Theoretical Chemistry Laboratory, Department of Chemistry, University of Oxford, Oxford OX1 3TA, U.K.;* Present Address: Refeyn Ltd., 1 Electric Avenue, Ferry Hinksey Road, Oxford OX2 0BY, U.K

Stephen Thorpe − *Physical and Theoretical Chemistry Laboratory, Department of Chemistry, University of Oxford, Oxford OX1 3TA, U.K.;* orcid.org/0000-0002-1601-7582

Robert W. Style − *ETH Zürich, 8092 Zürich, Switzerland;* orcid.org/0000-0001-5305-7658

Eric R. Dufresne − *ETH Zürich, 8092 Zürich, Switzerland;* orcid.org/0000-0002-3091-5039

Complete contact information is available at: https://pubs.acs.org/10.1021/acsphotonics.1c01268

Author Contributions

§X.M. and A.S.-S. contributed equally.

Notes

The authors declare no competing financial interest.

■ ACKNOWLEDGMENTS

P.K. is supported by an ERC Consolidator grant (PHOTOMASS 819593) and an EPSRC Leadership Fellowship (EP/T03419X/1), S.T. by the Emerson Collective, X.M. by the China Scholarship Council - University of Oxford scholarship, and A.S.-S. by a MCSA individual fellowship (INTFACDYN).

■ REFERENCES

(1) Shen, H.; Tauzin, L. J.; Baiyasi, R.; Wang, W.; Moringo, N.; Shuang, B.; Landes, C. F. Single Particle Tracking: From Theory to Biophysical Applications. *Chem. Rev.* **2017**, *117*, 7331−7376.

(2) Martin, D. S.; Forstner, M. B.; Käs, J. A. Apparent Subdiffusion Inherent to Single Particle Tracking. *Biophys. J.* **2002**, *83*, 2109−2117.

(3) Li, T.; Kheifets, S.; Medellin, D.; Raizen, M. G. Measurement of the Instantaneous Velocity of a Brownian Particle. *Science (Washington, DC, U. S.)* **2010**, *328*, 1673−1675.

(4) Huang, R.; Chavez, I.; Taute, K. M.; Lukić, B.; Jeney, S.; Raizen, M. G.; Florin, E.-L. Direct Observation of the Full Transition from Ballistic to Diffusive Brownian Motion in a Liquid. *Nat. Phys.* **2011**, *7*, 576−580.

(5) Balzarotti, F.; Eilers, Y.; Gwosch, K. C.; Gynnå, A. H.; Westphal, V.; Stefani, F. D.; Elf, J.; Hell, S. W. Nanometer Resolution Imaging and Tracking of Fluorescent Molecules with Minimal Photon Fluxes. *Science (Washington, DC, U. S.)* **2017**, *355*, 606−612.

(6) Juette, M. F.; Bewersdorf, J. Three-Dimensional Tracking of Single Fluorescent Particles with Submillisecond Temporal Resolution. *Nano Lett.* **2010**, *10*, 4657−4663.

(7) Isojima, H.; Iino, R.; Niitani, Y.; Noji, H.; Tomishige, M. Direct Observation of Intermediate States during the Stepping Motion of Kinesin-1. *Nat. Chem. Biol.* **2016**, *12*, 290−297.

(8) Maier, S. A. *Plasmonics: Fundamentals and Applications*; Springer Science & Business Media: 2007.

(9) Ueno, H.; Nishikawa, S.; Iino, R.; Tabata, K. V.; Sakakihara, S.; Yanagida, T.; Noji, H. Simple Dark-Field Microscopy with Nanometer Spatial Precision and Microsecond Temporal Resolution. *Biophys. J.* **2010**, *98*, 2014−2023.

(10) Weigel, A.; Sebesta, A.; Kukura, P. Dark Field Microspectroscopy with Single Molecule Fluorescence Sensitivity. *ACS Photonics* **2014**, *1*, 848−856.

(11) Ando, J.; Nakamura, A.; Visootsat, A.; Yamamoto, M.; Song, C.; Murata, K.; Iino, R. Single-Nanoparticle Tracking with Angstrom Localization Precision and Microsecond Time Resolution. *Biophys. J.* **2018**, *115*, 2413−2427.

(12) Lin, Y. H.; Chang, W. L.; Hsieh, C. L. Shot-Noise Limited Localization of Single 20 Nm Gold Particles with Nanometer Spatial Precision within Microseconds. *Opt. Express* **2014**, *22*, 9159−9170.

(13) Young, G.; Kukura, P. Interferometric Scattering Microscopy. *Annu. Rev. Phys. Chem.* **2019**, *70*, 301−322.

(14) Taylor, R. W.; Sandoghdar, V. Interferometric Scattering Microscopy: Seeing Single Nanoparticles and Molecules via Rayleigh Scattering. *Nano Lett.* **2019**, *19*, 4827−4835.

(15) Taylor, R. W.; Mahmoodabadi, R. G.; Rauschenberger, V.; Giessl, A.; Schambony, A.; Sandoghdar, V. Interferometric Scattering Microscopy Reveals Microsecond Nanoscopic Protein Motion on a Live Cell Membrane. *Nat. Photonics* **2019**, *13*, 480−487.

(16) Squires, A. H.; Lavania, A. A.; Dahlberg, P. D.; Moerner, W. E. Interferometric Scattering Enables Fluorescence-Free Electrokinetic Trapping of Single Nanoparticles in Free Solution. *Nano Lett.* **2019**, *19*, 4112−4117.

(17) Jacobsen, V.; Stoller, P.; Brunner, C.; Vogel, V.; Sandoghdar, V. Interferometric Optical Detection and Tracking of Very Small Gold Nanoparticles at a Water-Glass Interface. *Opt. Express* **2006**, *14*, 405.

(18) Ortega Arroyo, J.; Cole, D.; Kukura, P. Interferometric Scattering Microscopy and Its Combination with Single-Molecule Fluorescence Imaging. *Nat. Protoc.* **2016**, *11*, 617−633.

(19) Kukura, P.; Celebrano, M.; Renn, A.; Sandoghdar, V. Imaging a Single Quantum Dot When It Is Dark. *Nano Lett.* **2009**, *9*, 926−929.

(20) Kukura, P.; Celebrano, M.; Renn, A.; Sandoghdar, V. Single-Molecule Sensitivity in Optical Absorption at Room Temperature. *J. Phys. Chem. Lett.* **2010**, *1*, 3323−3327.
(21) Kukura, P.; Ewers, H.; Müller, C.; Renn, A.; Helenius, A.; Sandoghdar, V. High-Speed Nanoscopic Tracking of the Position and Orientation of a Single Virus. *Nat. Methods* **2009**, *6*, 923−927.
(22) Mashanov, G. I.; Tacon, D.; Knight, A. E.; Peckham, M.; Molloy, J. E. Visualizing Single Molecules inside Living Cells Using Total Internal Reflection Fluorescence Microscopy. *Methods* **2003**, *29*, 142−152.
(23) Mickolajczyk, K. J.; Hancock, W. O. High-Resolution Single-Molecule Kinesin Assays at kHz Frame Rates. In *Methods in Molecular Biology*; Humana Press Inc.: 2018; Vol. *1805*, pp 123−138.
(24) Lieb, M. A.; Zavislan, J. M.; Novotny, L. Single-Molecule Orientations Determined by Direct Emission Pattern Imaging. *J. Opt. Soc. Am. B* **2004**, *21*, 1210−1215.
(25) Brokmann, X.; Coolen, L.; Hermier, J. P.; Dahan, M. Emission Properties of Single CdSe/ZnS Quantum Dots Close to a Dielectric Interface. *Chem. Phys.* **2005**, *318*, 91−98.
(26) Lee, K. G.; Chen, X. W.; Eghlidi, H.; Kukura, P.; Lettow, R.; Renn, A.; Sandoghdar, V.; Götzinger, S. A Planar Dielectric Antenna for Directional Single-Photon Emission and near-Unity Collection Efficiency. *Nat. Photonics* **2011**, *5*, 166−169.
(27) Van Dijk, M. A.; Tchebotareva, A. L.; Orrit, M.; Lippitz, M.; Berciaud, S.; Lasne, D.; Cognet, L.; Lounis, B. Absorption and Scattering Microscopy of Single Metal Nanoparticles. *Phys. Chem. Chem. Phys.* **2006**, *8*, 3486−3495.
(28) Binks, B. P. Particles as Surfactants—Similarities and Differences. *Curr. Opin. Colloid Interface Sci.* **2002**, *7*, 21−41.
(29) Dickinson, E. Food Emulsions and Foams: Stabilization by Particles. *Curr. Opin. Colloid Interface Sci.* **2010**, *15*, 40−49.
(30) Tao, A.; Sinsermsuksakul, P.; Yang, P. Tunable Plasmonic Lattices of Silver Nanocrystals. *Nat. Nanotechnol.* **2007**, *2*, 435−440.
(31) Lin, Y.; Skaff, H.; Böker, A.; Dinsmore, A. D.; Emrick, T.; Russell, T. P. Ultrathin Cross-Linked Nanoparticle Membranes. *J. Am. Chem. Soc.* **2003**, *125*, 12690−12691.
(32) Pickering, S. U. CXCVI.—Emulsions. *J. Chem. Soc., Trans.* **1907**, *91*, 2001−2021.
(33) Ramsden, W.; Gotch, F. Separation of Solids in the Surface-Layers of Solutions and 'Suspensions' (Observations on Surface-Membranes, Bubbles, Emulsions, and Mechanical Coagulation).—Preliminary Account. *Proc. R. Soc. London* **1904**, *72*, 156−164.
(34) Pieranski, P. Two-Dimensional Interfacial Colloidal Crystals. *Phys. Rev. Lett.* **1980**, *45*, 569−572.
(35) Bresme, F.; Oettel, M. Nanoparticles at Fluid Interfaces. *J. Phys.: Condens. Matter* **2007**, *19*, 413101.
(36) Wang, D.; Hu, R.; Skaug, M. J.; Schwartz, D. K. Temporally Anticorrelated Motion of Nanoparticles at a Liquid Interface. *J. Phys. Chem. Lett.* **2015**, *6*, 54−59.
(37) Scriven, L. E.; Sternling, C. V. The Marangoni Effects. *Nature* **1960**, *187*, 186−188.
(38) Crocker, J. C.; Valentine, M. T.; Weeks, E. R.; Gisler, T.; Kaplan, P. D.; Yodh, A. G.; Weitz, D. A. Two-Point Microrheology of Inhomogeneous Soft Materials. *Phys. Rev. Lett.* **2000**, *85*, 888−891.
(39) Prasad, V.; Weeks, E. R. Two-Dimensional to Three-Dimensional Transition in Soap Films Demonstrated by Microrheology. *Phys. Rev. Lett.* **2009**, *102*, 178302.
(40) Di Leonardo, R.; Keen, S.; Ianni, F.; Leach, J.; Padgett, M. J.; Ruocco, G. Hydrodynamic Interactions in Two Dimensions. *Phys. Rev. E* **2008**, *78*, 31406.
(41) Diamant, H. Hydrodynamic Interaction in Confined Geometries. *J. Phys. Soc. Jpn.* **2009**, *78*, 41002.
(42) Young, G.; Hundt, N.; Cole, D.; Fineberg, A.; Andrecka, J.; Tyler, A.; Olerinyova, A.; Ansari, A.; Marklund, E. G.; Collier, M. P.; Chandler, S. A.; Tkachenko, O.; Allen, J.; Crispin, M.; Billington, N.; Takagi, Y.; Sellers, J. R.; Eichmann, C.; Selenko, P.; Frey, L.; Riek, R.; Galpin, M. R.; Struwe, W. B.; Benesch, J. L. P.; Kukura, P. Quantitative Mass Imaging of Single Biological Macromolecules. *Science (Washington, DC, U. S.)* **2018**, *360*, 423−427.
(43) He, Y.; Lin, S.; Marc Louis Robert, H.; Li, H.; Zhang, P.; Piliarik, M.; Chen, X. W. Multiscale Modeling and Analysis for High-Fidelity Interferometric Scattering Microscopy. *J. Phys. D: Appl. Phys.* **2021**, *54*, 274002.

https://doi.org/10.1021/acsphotonics.1c01268
ACS Photonics 2021, 8, 3111−3118